Quantifying Processing Map Uncertainties by Modelling the Hot-Compression Behaviour of a Zr-2.5Nb Alloy

Christopher S. Daniel[1*], Patryk Jedrasiak[2], Christian J. Peyton[1], João Quinta da Fonseca[1], Hugh R. Shercliff[2], Luke Bradley[3], Peter D. Honniball[3]

[*]Corresponding author – christopher.daniel@manchester.ac.uk

[1]Centre for Light Alloy Research and Innovation, The University of Manchester, Oxford Road, Manchester, M13 9PL, UK

[2]Department of Engineering, University of Cambridge, Trumpington Street, Cambridge, CB2 1PZ, UK

[3]Rolls-Royce plc, Derby, DE21 7XX, UK

Abstract

Compression dilatometer tests were used to study the hot deformation response of a Zr-2.5Nb alloy over the temperature range 650°C – 850°C and strain rates of $10^{-2.5}$ s^{-1} – 10^{+1} s^{-1}. A high number of test conditions was used (72, with every test duplicated), in order to assess how differences in data processing influence the resulting relationships between flow stress, temperature and strain-rate. Particular attention was paid to 'processing maps', showing strain-rate sensitivity over the processing domain, commonly cited in the field and widely used as a basis to determine optimum processing conditions. Significant variations in these maps were found to depend on the number of data-points included and the fitting procedure used to smooth the data. A finite element (FE) model of the test demonstrates the order of the corrections that can be required to the flow stress and the consequent processing maps due to friction at the platen-workpiece interface, and non-uniform temperature and deformation in the test piece. Changes in crystallographic texture, measured using electron-backscatter diffraction (EBSD), illustrate the effect of temperature, strain and strain-rate on the deformation, phase transformation and recrystallization mechanisms. A significant spread in response arises as a result of variation in micro-texture between samples and the tendency for flow to localise, giving rise to scatter in the measurements and generating artefacts in the

processing map. Although the processing map methodology is strongly affected by experimental uncertainty, a detailed analysis of the final microstructures in the test samples show similar features to those produced during industrial-scale processing, providing insight into the deformation mechanisms in dual-phase Zr-Nb alloys.

Keywords

alpha beta processing, zirconium, compression testing, processing maps

1. Introduction

The specific thermomechanical processing route for Zr alloys is chosen to control the development of microstructures and favoured crystallographic orientations (textures), which greatly affect the mechanical properties of nuclear reactor components in-service [1,2]. For the use of stronger dual-phase Zr-Nb alloys in new nuclear applications [3], containing both α (hcp, hexagonal close-packed) and β (bcc, body-centred-cubic) phases, a better understanding of the effect of processing parameters on two-phase microstructure and texture evolution during high temperature deformation is required, to minimise process development costs and for optimisation of the processing route.

In an ideal process optimisation study, the microstructure evolution would be studied by characterising the material deformed under well-controlled process conditions. But, since the stress-strain response of a material is affected by the constitutive behaviour and microstructural evolution, it has been suggested that the stress-strain behaviour alone could be used to determine the optimum processing conditions. This is the idea behind the processing map tool proposed by Prasad et al., based on the approach of dynamic materials modelling (DMM) [4,5]. In this approach, effective processing conditions are those that maximise the 'power dissipation' term η, which describes the partitioning of deformation energy between dissipated heat and storage through microstructural changes in the material [6]. η is defined as $m/(1+m)$ and therefore maximizing η is equivalent to maximizing the strain rate sensitivity, m. Processing maps have been widely used to determine the optimum hot deformation regimes in all materials, including Zr alloys [7–20] and Ti alloys [21–26], in studies where observations of the final microstructures at room temperature are used to validate the process map. The processing map approach has become even more popular recently, with the wider availability of thermomechanical simulators like the Gleeble and compression dilatometers, which

significantly speed up compressive testing. These machines make it very easy to rapidly produce process maps and quickly assess new alloys for processability, which has led to an explosion in the number of process map studies for all kinds of alloys and composites.

Despite its popularity and wide acceptance there are significant shortcomings with using the process map methodology to identify processing conditions. There has been strong criticism of the DMM approach underpinning the method. It has been called too simple to account for the complexity of the many deformation and microstructure evolution processes involved [6,27,28]. Many recent articles avoid using the power dissipation term from the DMM approach and instead create processing maps using only strain rate sensitivity values, which are almost equivalent. It is plausible that a high strain rate sensitivity might identify deformation conditions where non-conservative mechanisms are active, involving grain and phase boundary movement, for example [13,16,20,29–33]. However, obtaining strain rate sensitivity variation using the methodology proposed is fraught with difficulties which are very often ignored or given only cursory attention. The method relies on data from hot uniaxial compression tests, during which the deformation conditions always vary across the sample in ways that depend on the details of the experimental setup. Although the data is often 'corrected' [12,30], details of these corrections are often not given. Furthermore, the material tested often has large microstructural features of sizes comparable to those of the samples tested [12], which cause experimental scatter, but that is either ignored or not reported. One of the consequences is that although the processing map methodology is very popular, reproducibility is very poor. For example, the contour maps for Zr-2.5Nb alloy in the low strain rate regime (10^{-3} to 10^{-2} s^{-1}), show many different maximum values for m formed at either 710°C to 830°C [16], 730°C [15], 750°C [11], 770°C to 900°C [16], 900°C [11], 920°C to 1020°C [12] and 950°C [15].

The aim of this study was to critically assess whether the processing map approach can be used to predict microstructural development in Zr-2.5Nb and identify ideal process conditions. The process map methodology was used but with many more tests than is usual and repetitions at each condition. A finite element (FE) model of the tests was used to evaluate the effects of friction and thermal gradient and the resultant inhomogeneous deformation. This paper explores these factors, and highlights the variations in outcome that can arise in interpreting flow stress data to develop process maps, purely derived from differences in analysis method.

It then tests processing map predictions by comparing the microstructures of samples deformed under different conditions.

2. Compression Dilatometer Tests

2.1 Starting Material

The material studied was a Zr-2.5Nb alloy specially produced at Wah Chang Corporation to obtain a small prior-β grain size. This was achieved through forging of a 27" diameter ingot into a 5" thick slab, which was then hot-rolled to 3" thick and finally machined to a starting material block, shown in Figure 1 a). The β-transus in the starting Zr-2.5Nb material was recorded at 890°C, determined by length changes measured on the DIL 805 A/D/T quenching and deformation dilatometer during an inductive heating cycle at 1.5°C/s. The initial forged microstructure was air-cooled from just above the β-transus, resulting in a microstructure of Widmanstätten packets of α-laths, as shown in Figure 1 c) and d), separated by fine filaments of retained metastable β_{Zr} [34]. Analysis of the starting material shows prior-β grains covering an average area of $0.59 \pm 0.04\,\mathrm{mm}^2$ with a diameter of $0.75 \pm 0.03\,\mathrm{mm}$, which are significantly smaller compared with previous hot-deformation studies on Zr-2.5Nb [12].

A number of cylindrical specimens measuring $10\,\mathrm{mm}$ in height and $5\,\mathrm{mm}$ in diameter were machined from the forged block, as shown schematically in Figure 1 b) with orientation relative to the plate. These were cut with a starting texture such that the α-phase basal pole maxima is initially aligned parallel with the compression direction (CD), along the longitudinal axis of the sample, as shown in Figure 2. A map of the indexed α orientations, as slices taken from cross-sections of the sample, are shown in the radial (R1, R2) plane and in the CD-R2 plane. Also shown are reconstructed maps of the larger β-grains formed at high temperature, determined using a β-phase reconstruction software developed by Davies et al. [35–38].

2.2 Hot-Compression Testing

Compression tests were carried out using TA Instruments DIL 805 A/D/T quenching and deformation dilatometer. A disadvantage of other high temperature compression rigs is that a furnace is usually used to heat samples, which is time-consuming and expensive. Temperature on the dilatometer is instead controlled through induction heating of samples, which has the

advantage of providing fast heating and cooling rates, with minimum sample changeover time between tests, for quick investigation of a large hot-compression matrix.

Test temperatures were chosen to cover the range over which the α/β volume fraction changes with temperature [39]. Temperature was monitored using a S-type thermocouple, welded at mid-length on each specimen. Compression tests were conducted at temperatures, T, of 650, 675, 700, 725, 750, 775, 800, 825 and 850℃. Tests were conducted in an inert He gas atmosphere to minimise sample oxidation. The specimens were heated to the deformation temperature at $5\,℃/\mathrm{s}$ and held for 3 minutes to homogenise the temperature. At each temperature, tests were conducted at constant strain rate, $\dot{\varepsilon}$, of $10^{-2.5}$, 10^{-2}, $10^{-1.5}$, 10^{-1}, $10^{-0.5}$, 10^{+0}, $10^{+0.5}$ and 10^{+1} s^{-1} to a true strain, ε, of 0.69 (corresponding to 50% height reduction). Tests were also repeated at each condition. In order to minimise frictional stresses generated during deformation, a graphite and nickel lubricant was applied between the specimen and the silicon nitride (Si_3N_4) compression platens. Heat loss to the silicon nitride platens was found to contribute to a $50℃ - 100℃$ temperature difference from the edge to the centre of the compression sample. Immediately after the hot-compression test, specimens were cooled at a rate of $5\,℃/s$ and the recorded data converted to true stress and true strain plots.

2.3 Data Repository

All experimental data is available from the Zenodo repository, along with an accompanying python script to generate the plots [40].

2.4 True Stress-Strain Response

The convention in compression testing is to convert the measured force-displacement response to true stress-strain, assuming homogeneous frictionless deformation:

$$\sigma_{true} = \frac{F}{\pi D^2} \quad \text{and} \quad \varepsilon_{true} = ln\frac{H}{H_0}$$

Equation 1

The instantaneous diameter, D, is calculated from the height, H, the original diameter, D_0, and the original height, H_0, using volume conservation. Figure 3 a) and b) show the idealised shape change assumed in Equation 1; in contrast, Figure 3 c) shows a predicted sample shape with barrelling due to friction and a non-uniform temperature. It is still convenient to convert the force-displacement data using Equation 1, using a notional average diameter as calculated as

usual, for example to compare test data FE predictions and published constitutive data. Test data presented in this way will be referred to as 'notional' true stress-strain curves, to distinguish between these and a corrected constitutive response. Figure 4 a) shows a sample of measured force-displacement curves at a constant temperature for various strain-rates, and the corresponding true stress (σ) versus true strain (ε) responses.

The experimentally measured true stress-true strain responses are shown in Figure 4 b) and c), showing the effect of different temperatures at constant strain rate ($10^{-2.5}$ s^{-1}) and different strain rates at constant temperature ($800℃$), with the complete data set available in the repository [40]. The yield strength shows a clear trend with strain rate and temperature, with higher material strength at low temperatures and high applied strain rates. Following peak stress, the curves indicate that the material undergoes flow softening. All curves exhibit flow softening to a degree, although the amount varies with temperature, as well as with strain rate. The largest reduction in flow stress is recorded at $650℃$. Continuous 'apparent' flow softening always appears at higher strain rates ($\dot{\varepsilon} > 10^{+0}$ s^{-1}), along with flow softening exhibited in all tests at temperatures up to 800°C up to the largest strain increment ($\varepsilon = 0.69$). Near steady state behaviour is only reached in the majority of tests at $825℃$ and $850℃$. These characteristics of flow softening are commonly observed during deformation in the α + β regime of Zr and Ti alloys with starting lamellar microstructure [12,15,16,24,30,31].

The repeatability in most cases is very good, with variation between duplicates of the order of 5% – 10%, which may reflect real microstructural variation, rather than experimental variability. The flow behaviour is mostly reproduced in the majority of repeat tests, although there are noticeable differences in the flow stresses at some conditions. The uncertainty is greatest at low temperatures and high strain rates, when the flow curves exhibit some sharp variations in stress over time. Although the majority of raw data shows relatively smooth flow stress behaviour, a few tests at lower strain rates also showed occasional sharp drops in stress. Even at the highest temperatures, when the flow curves appear smooth and closely replicated, differences of around 5 MPa exist between samples. Therefore, for the purposes of fitting an average response, two flow stress data-points were extracted for analysis at a given strain in each given test.

2.5 Microstructural Analysis

Analysis of the microstructures and crystallographic textures of the Zr-2.5Nb alloys were made on the deformed specimens after sectioning parallel to the compression axis. Following sectioning, samples were mounted in Bakelite and ground using wet silicon carbide abrasive papers with 600 and 800 grit, followed by 6 μm and 1 μm diamond mechanical polishing, with a final polish using a $5{:}\,1$ solution of colloidal silica/hydrogen peroxide.

Macro-texture measurements of the selected regions, before and after deformation, were performed using electron backscatter diffraction (EBSD) on the FEI CamScan MX2000 field emission gun scanning electron microscope (FEG-SEM) and TESCAN MIRA3 FEG-SEM. EBSD data was collected at an operating voltage of 20 kV with a working distance of 27 mm for the CamScan and 20 mm for the TESCAN. Both systems are equipped with AZtecHKL EBSD systems for pattern indexing, with subsequent analysis performed using Channel 5 software.

For the initial measurement of the starting forged material texture, a 5 μm step size was chosen and a total area of $145\ \mathrm{mm}^2$ analysed. Following compression, macro-texture maps of the deformed samples were also recorded at a step size of 5 μm, over the entire surface parallel to the compression axis, in the R1-CD plane. Texture changes were measured both across the entire specimen and located within a deformed band at the centre, covering a rectangular area of about 5×1 mm. Fine microstructure orientation maps were also recorded at the centre of samples following deformation at different strain rates of $10^{+0}\ \mathrm{s}^{-1}$ and $10^{-2.5}\ \mathrm{s}^{-1}$ at 800℃, using a step size of 0.25 μm to index both the α and β phases and to investigate the differences in grain structure.

The images of compression samples deformed at 700℃, 800℃ and 850℃ at strain rates of $10^{+0}\ \mathrm{s}^{-1}$ and $10^{-2.5}\ \mathrm{s}^{-1}$ are shown in Figure 5. The microstructures show clear evidence of non-uniform straining, with undeformed material in the form of 'dead metal zones' (DMZs) at the top and bottom of the sample, retaining the large prior-β grain structures from the starting material. Heavily deformed regions localise at the centre. The different combinations of deformation parameters (temperatures and strain rate) contribute to the extent of non-uniform strain gradients, affecting flow localisation at the centre and barrelling of the edges. Flow localisation at the centre appears to increase at higher deforming temperatures, at 800℃ and

850℃, leading to extensive breakdown of the starting prior-β grain structures, which is also most significant at lower strain rates of $10^{-2.5}\ s^{-1}$. At 700℃, and at both $10^{+0}\ s^{-1}$ and $10^{-2.5}\ s^{-1}$, the sample centre contains larger individual prior-β grains which are less deformed, suggesting a more homogenous strain gradient and less localisation. Throughout the samples the dependence of the macro-scale deformation on interaction of large prior-β grain regions, along with strain localisation at grain boundaries, is evident. In some cases, whole prior-β grain regions are seen to slide out from the barrelled surface, most clearly seen at the top right of the specimens in Figure 5 c), as well as in the bottom right of Figure 5 d).

The strain gradient in the sample is reflected in the variation of the α crystallographic orientation across the sample, as shown after deformation at 850℃ and $10^{-2.5}\ s^{-1}$ in Figure 5 e). In the DMZs, each prior-β grain retains the different α variant orientations. However, at the centre, in the region of localised flow, the α orientations develop a weak texture, aligning the $\langle 11\bar{2}0 \rangle$ parallel to CD and forming the 0002 basal pole with maxima in R1 and R2, along with a spread throughout the radial plane.

3. Finite Element (FE) Modelling of Hot-Compression Tests

Finite element analysis was used to assess the influence of inhomogeneous deformation in the dilatometer tests, in particular the apparent shift in true stress-strain behaviour due to friction under the platens, and a temperature gradient due to heat loss to the platens. Capturing the non-uniform temperature field requires a full heat transfer analysis of the dilatometer rig. This is challenging, as the control system includes both induction heating and forced inert gas cooling to manage the sample temperature, heat losses occur into the loading platens, while plastic dissipation adds a further non-uniform internal heat source. Furthermore, a single central thermocouple does not provide sufficient information to calibrate the heat transfer conditions between the sample and the platens. This study therefore involved a parametric investigation of the effect of friction and temperature gradient, using simplified boundary conditions.

3.1 Modelling Methodology

A numerical scheme was developed for inferring the uniaxial true stress-strain response, by applying a systematic correction to the 'notional' true stress-strain response taken directly from the test data, accounting for the influence of friction and inhomogeneous temperature. The procedure is illustrated in Figure 6, summarised as follows:

(a) take a first estimate for the constitutive response, $\sigma = f(T, \dot{\varepsilon}, \varepsilon)$, as input to the FE analysis, predicting the force-displacement for the test matrix, and converting to notional true stress-strain (as for the experimental response, using Equation 1);
(b) at a number of discrete strains, evaluate the *offset* in stress, $\Delta\sigma = f(T, \dot{\varepsilon})$, caused by friction and a temperature gradient;
(c) *subtract* this $\Delta\sigma$ from the experimental notional true stress-strain data, to give a corrected input dataset for $\sigma = f(T, \dot{\varepsilon}, \varepsilon)$, and use this to re-predict the experimental curves (in the form of notional true stress-strain), to validate the corrected constitutive data.

3.2 FE Mesh and Thermal Boundary Conditions

The axisymmetric mesh and initial dimensions are shown in Figure 7, along with the idealised temperature boundary conditions. The temperature gradient was not measured in-situ for the Zr-2.5Nb alloy. Nevertheless, similar tests using a Ti-6Al-4V alloy, under similar conditions using the same dilatometer, indicate peak gradients of the order $50℃ - 100℃$, which reduce during the test as the sample shortens. It is reasonable to expect a similar temperature gradient to appear in the Zr-2.5Nb alloy, since it is mostly affected by heat conduction to the loading platens and Zr-2.5Nb has a similar thermal conductivity to Ti-6Al-4V ($17.1\,\mathrm{W/mK}$ compared with $7.1\,\mathrm{W/mK}$). The central temperature is well-maintained by the dilatometer, up to strain-rates around $1\ \mathrm{s}^{-1}$, above which adiabatic heating by plastic dissipation leads to a rise in the central temperature. In the current work, in the absence of temperature data from the Zr-2.5Nb instrumented tests, a gradient was maintained from the nominal test temperature at the centre of the sample to a fixed temperature below nominal at the platen interface.

Friction is difficult to measure, so a constant friction coefficient was applied in the model and treated as an adjustable parameter. It is found that beyond a value of $\mu \approx 0.5$, the radial spread at the platen is small, and there is little sensitivity to the value of μ. A sensitivity analysis was conducted to explore the influence of friction and the imposed temperature difference, with the final sample shape providing a qualitative comparator with the experiments (as in Figure 5). This analysis included the usual checks on mesh sensitivity and convergence, and details are available elsewhere [41]. The results presented in this paper apply a friction coefficient $\mu = 0.5$, and a temperature difference of $100℃$, which represent a 'worst case' upper bound, as a proof of concept.

3.3 Constitutive Data

The methodology addresses something of a circular problem – correcting the stress-strain response requires a reasonable first estimate of the constitutive response, to use as an input to the FE analysis. Options for this first estimate are: (a) true stress-strain constitutive response from the literature, if available and reliable; (b) a dataset for $\sigma = f(T, \dot{\varepsilon}, \varepsilon)$ that is extracted from the experimental data. Since the objective is to find the *offset* in the data $\Delta\sigma = f(T, \dot{\varepsilon}, \varepsilon)$, due to friction and a temperature gradient, it is reasonable to assume that this correction will be insensitive to the absolute values used as input, provided the flow stress and its variation $\sigma = f(T, \dot{\varepsilon}, \varepsilon)$ cover the same processing domain as the experiments.

An isotropic plastic response for the Zr-2.5Nb alloy was assumed, in spite of its strong texture and complex phase transformations, as the goal is to capture the first-order effects of friction and temperature gradient – hence an isotropic average constitutive response is sufficient. The initial FE analysis used a perfectly-plastic (strain-independent) fit to the raw data at a low strain $\varepsilon = 0.05$. This implementation was used for setting up the FE model as outlined previously (e.g. for checks on convergence and mesh size, and the sensitivity analysis on friction and temperature gradient [41]).

For the full analysis of the correction to flow stress, it was preferable to avoid loss of detail by curve-fitting directly to the experimental data *before* they had been compensated for inhomogeneity in deformation. The analysis therefore reverted to a full look-up table for flow stress $\sigma = f(T, \dot{\varepsilon}, \varepsilon)$, using the 'notional' true stress-strain curves directly, rather than a perfectly-plastic response. This still required judicious 'smoothing' of the experimental data (to avoid introducing artefacts in the data, such as local non-physical fluctuations in strain-rate sensitivity). The data were extracted at discrete strains at intervals of 0.05, and second-order surface fits were used to find $\sigma = f(T, \dot{\varepsilon})$ at each strain, taking account of the scatter between repeat experiments. Smoothing of point-to-point fluctuations in the raw experimental data is best conducted as a simultaneous *surface* fit in both T and $\dot{\varepsilon}$, since fitting at an isolated temperature or strain-rate readily introduces non-physical artefacts, such as cross-over of curves at different T or $\dot{\varepsilon}$. The goal was therefore to achieve a surface fit for flow stress $\sigma = f(T, \dot{\varepsilon})$, with smooth continuous gradients and curvature, while using the lowest order fit

possible, to avoid any over-fitting. Note that these arguments also apply to the generation of processing maps, considered later in the paper.

3.4 Correction using FE Model

A 2×2 matrix of tests was chosen with conditions that fell inside the upper and lower limits of both temperature and strain-rate: 700℃ and 800℃, 10^{-2} s^{-1} and $10^{+0.5}$ s^{-1}, subsequently expanded to a 3×3 matrix with an intermediate T and $\dot{\varepsilon}$. The real tests experience T and $\dot{\varepsilon}$ distributions above and below the nominal test value, so narrowing the test matrix for the FE analysis limited the uncertainty caused by extrapolation beyond the ranges of the input constitutive data.

Figure 6 shows FE results taken from the 2×2 matrix of conditions: the input and output stress-strain responses, indicating the stress offset $\Delta\sigma$; and the corrected constitutive data, with the predicted and experimental 'notional' true stress-strain curve. The correction methodology works well, only requiring a single iteration to generate a corrected look-up table for $\sigma = f(T, \dot{\varepsilon}, \varepsilon)$. Note that the magnitude of the correction varies with strain, so that the interpretation of the extent of work softening may be significantly modified, as well as the magnitude of the flow stress. The analysis was then conducted over the 3×3 temperature and strain-rate matrix, at every strain up to 0.6 in intervals of 0.05. It is not claimed that this yields a definitive constitutive response, since the correction applied depends on the temperature gradient and friction coefficient. But, the analysis demonstrates that there is a significant influence on the true stress-strain response of the inhomogeneity in the deformation. A more accurate correction could be made, given a better knowledge of the temperature distribution, via experiment and heat flow modelling.

The FE model in its current form can be used for further analyses, for example, to estimate the discrepancy between the nominal test conditions and those experienced in the central region of the sample. Figure 8 shows a number of predicted distributions in local conditions at the end of the deformation stage, for a high strain-rate (1 s^{-1}) at a test temperature $T = 800$℃ at the centre of the sample, with a temperature gradient of 100℃. The plots of strain and strain-rate show good qualitative equivalence with the experimentally observed deformation in Figure 5 c), with clear 'dead-metal zones' (DMZs), and deformation concentrated in the mid-plane of

the sample. A semi-quantitative comparison can be made with the extent of barrelling, characterised by the ratio of the maximum cross-section area to that of the notional cross-section area in the absence of barrelling – as in Figure 3 b) and c). Figure 9 shows a 'heat map' fitted to the experimental data, and to the corresponding predictions of the FE analysis. The trend of increased barrelling from top left to bottom right is captured well, with reasonable quantitative agreement.

Figure 8 shows that the local strains and strain-rates in the centre of the sample are approximately 4 to 5 times higher than the nominal values. From equivalent output at other strain-rates, it is apparent that the kinematic self-similarity on the deformation means that this factor is almost independent of the imposed strain-rate, in part because the imposed temperature profile is identical in all cases. The analysis demonstrates therefore that microstructural interpretation of dilatometer samples (or, equally, deeper analyses of the central region using crystal plasticity) must take due account of the inhomogeneity in the deformation conditions.

A further application of the FE corrected flow stress data is in the extraction of material characteristics from the constitutive data – such as strain-rate sensitivity – as presented in the literature as 'processing maps'. This is investigated in the next section, following a study of the influences of data sampling procedures on the form of these maps.

4. Discussion

4.1 Strain Rate Sensitivity 'Processing Maps'

The standard procedure for obtaining strain rate sensitivity (processing) maps is as follows [12]:

- Obtain flow stress values from experimental stress-strain curves at a pre-determined strain value (usually 0.5)
- Fit cubic polynomials to $\log(\sigma)$ vs $\log(\dot{\varepsilon})$ values at each constant temperature
- Differentiate the cubic polynomials to obtain the strain rate sensitivity m
- Plot m on a map of $\log(\dot{\varepsilon})$ against temperature

The results of this analysis are shown for the uncorrected data in Figure 10 a). The overall trend is an increase in strain rate sensitivity with decreasing strain rate and increasing temperature. The analysis yields negative strain rate sensitivity values for tests at low temperatures and high strain rates, which may be a consequence of adiabatic heating and/or non-uniform conditions in the sample, or could be a numerical artefact due to the data sampling. In previous studies, adiabatic heating is corrected for using a variety of different methods [12,15,16,42,43]. Here, the thermocouple on the sample measured a 50 K temperature spike during the initial stages of deformation at the highest strain rates, which is eliminated during the test by the temperature controller on the dilatometer. Nevertheless, the initial temperature spike may be sufficient to induce permanent softening in these samples, producing apparent negative strain rate sensitivity.

The process map has a clear peak in strain rate sensitivity at $775℃$, which would indicate optimum processing conditions. Peaks at $750℃ - 775℃$ have been reported by other researchers [11,15,16], however, it is difficult to compare process maps directly since the maps are plotted differently, and the regimes change when they cover different process parameter ranges [12,18]. They also invariably contain fewer measurement points (5 temperatures and strain rates and sometimes fewer), with no repeated tests. To illustrate the variability in the map due to the size of the dataset, subsets of the data produced here were used to produce process maps using only 5 different strain rates at each temperature. The resultant maps are shown in Figure 10 b) and c). These show that reducing the number of points noticeably changes the appearance of the processing map: it changes the values of the maximum and minimum strain rate measured and moves the position of the high strain rate sensitivity peak by as much as $50℃$. This is a direct consequence of using a cubic polynomial with only 5 experimental points, of what is, unavoidably, somewhat noisy data. Interestingly, one of these new maps (Figure 10 b)) agrees reasonably well with the map from the data by Chakravartty et al. [12], shown in Figure 10 d), unlike the original map with all the data points which looked quite different.

To explore the effect of measurement uncertainty on individual measurements on the final process map, random noise normally distributed over a ± 5 MPa range around the mean was added to the mean of the flow stresses measured at each condition. The results of this exercise are shown in Figure 11. Although all process maps show the same overall trend of increasing strain rate sensitivity with decreasing strain rate, the temperature at which peaks in *m* appear

varies, as do the calculated values. This variation in map appearance is consistent with the variation seen in the literature [11,12,15,16,18], but is again the consequence of using a cubic polynomial to fit the data. These maps use all the data points measured and the differences between the maps are even more noticeable if fewer points are measured.

The data used to produce these processing maps assumes ideal uniaxial compression conditions, which cannot be met during compression testing, especially at high temperatures where friction is always significant. New fast testing solutions like the Gleeble and the compression dilatometer used here introduce larger temperature gradients than in more conventional isothermal tests. In our case, and as demonstrated by the FE analysis, there are both clear friction and temperature effects that produce both a strain and strain rate gradient along the gauge. The most obvious manifestation of these effects is sample barrelling. In some processing map studies, a barrelling correction is applied to the results to account for the sample shape change during deformation and the development of triaxiality [42,44,45]. However, these corrections are insufficient, since as the FE simulations show the link between the macroscopic nominal stress-strain curve and the actual stress-strain curve of the material is not simple. In each test the macroscopic sample response is an average of the material behaviour over all the different conditions in the sample. The range of conditions within a sample depends on the experimental setup and the constitutive behaviour of the material. In materials with coarse microstructural features the magnitude of these effects will vary from sample to sample. This is evident in the results for the tests at $700℃$ as can be seen in the 'heat map' in Figure 9, where the barrelling varies significantly for samples tested at similar, relatively low strain rates. Because the processing map workflow involves fitting the data at different temperatures separately using a cubic polynomial, these effects propagate into the strain rate sensitivity map, producing a peak in m. It is, therefore, not surprising that process maps have poor repeatability.

In order to determine the true constitutive response of the material, data from the FE analysis was fitted using a *surface* fit in temperature strain-rate space, where it became clear that the scatter in the data did not justify the use of a polynomial of order higher than 2. Using this data to create a process map produces the map shown in Figure 10 e). The corrected data slightly decreases the gradient in strain rate sensitivity with temperature and completely removes the peaks in *m* between $725℃$ and $800℃$, yielding a smooth increase in strain rate sensitivity with increasing temperature and decreasing strain rate, peaking at $800℃$. The peak value of m at

800°C is somewhat higher than the measured values and could be a consequence of extrapolating beyond the calibration data at this extreme condition, where the strain and temperature gradients are highest and there is a lack of a correction at 850°C.

The variation in deformation conditions experienced within one sample are reflected in variations in the microstructure seen after the test. These variations in microstructure provide a range of opportunities to find evidence for the regime predicted by the process maps, which helps explain why many studies are successful in validating the approach via post-mortem microstructural analysis [7–26]. Very few articles contain full sample metallographic images like those shown in Figure 5, and only give limited consideration to the range of deformation conditions in the sample. However, strong emphasis is invariably given to examining the sample at the mid-section, away from the platens, which implies that the microstructure does vary significantly in all cases.

Given this deformation inhomogeneity, identifying the best region to study becomes very difficult since there is no volume for which the conditions are constant. This is made even more difficult by the presence of coarse microstructural features like grain boundary α that cause strain localization and introduce asymmetry to the deformation. Nevertheless, with the assistance of the FE simulations we can estimate the actual process conditions in the centre of the samples tested here. The predicted effective strain and strain rates at the midpoint of four of the samples are shown in Table 1. The predicted strain and strain rate values are some 2 to 5 times higher than the nominal test strain value. This implies that even if one is careful to analyse only the midsection of the sample, the microstructure observed will usually not correspond to the nominal test conditions identified in the process map. The difference in total deformation is most significant: whereas the assumed, nominal strain is 0.7, the actual strain can be as high as 4. Furthermore, the difference in the strain and strain rates increases with increasing temperature and decreasing strain rate, a consequence of the increasing strain rate sensitivity and its effect on increasing the deformation inhomogeneity observed in Figure 5.

These considerations make it difficult to analyse the microstructural changes in the samples tested, as shown in Figure 12. For example, it could be argued that at 800°C there is a trend towards more globularisation of the microstructure at the lower strain rates and at the same temperature, but since the total strain at the lower strain rate is twice that at the higher strain

rate, it is difficult to say this is purely a strain rate effect. In this case, strain rate is probably the main effect, since the microstructure changes only very slowly at large strains. There is a general trend towards more globularisation or recrystallization in the processing map conditions where the strain rate sensitivity is higher [20], but it is not possible to be more quantitative.

Table 1: Comparison between nominal strain (0.69) and strain rate and the finite element (FE) predicted strain and strain rate, at the centre of the sample at 700℃ and 800℃.

Temperature (℃)	Nominal Strain Rate (s^{-1})	FE Predicted Strain Rate (s^{-1})	FE Predicted Strain
700	10^{+0}	$10^{+0.5}$	1.6 – 2.0
700	$10^{-2.5}$	$10^{-1.9}$	2.8 – 3.2
800	10^{+0}	$10^{+0.6}$	2.8 – 3.2
800	$10^{-2.5}$	$10^{-1.9}$	3.6 – 4.0

Texture control is an important aim of the thermomechanical processing of Zr-2.5Nb, since it strongly affects in-reactor performance. The pole figures for the material at the mid-point of the samples are shown in Figure 13 for three different temperatures and two extreme nominal strain rates. There appears to be clear trends in the texture development, both with temperature and strain rate: the texture appears to be stronger at the higher strain rates and the 0002 poles seem to gradually align towards the radial directions as temperature increases and strain rate decreases. However, since the texture of this material is strongly affected by the amount of deformation [39], it cannot be determined whether these changes are driven by time-dependant strain rate changes or if they are simply a consequence of the higher level of strain reached at the lower strain rates.

The EBSD analysis confirms the observations from the metallographic examination. Figure 13 h) and i) shows two maps of the microstructure after deformation at 800℃. There is clearly more evidence for recrystallization/globularization in the material deformed at the lower strain rate, although it is noticeable that the recrystallized grains appear in clusters of similar orientation, the majority with 0002 basal poles aligned in the radial directions (perpendicular to the compression direction). Surprisingly, the β texture appears to be much stronger after deformation at the higher strain rate. The β texture develops a cube component, with 100||CD, which is unusual in lacking the axial symmetry expected for uniaxial compression, which could

be due to the inhomogeneity in deformation in the sample and the interaction of large prior β grains [3]. In Zr-2.5Nb deformed at 800°C, the texture is created during both deformation and phase transformation on cooling and therefore it cannot be completely determined by the deformation conditions.

Given the inhomogeneity of the dual-phase microstructures and textures, it is not surprising that there is little agreement in the ideal processing conditions for Zr-2.5Nb recommended in the literature [11,12,15,16]. The inhomogeneity of the deformation behaviour exacerbates two consequences within the processing map methodology. Firstly, the measurement reproducibility is affected, meaning the same ideal process conditions will rarely be predicted. Secondly, if a regime is identified for investigation, the deformation state of the material analysed, using optical microscopy or EBSD, is unlikely to correspond with the processing parameters recommended in the map, particularly if the ex-situ observations are made at the centre of the specimen. As these results show, optimal processing regimes can only be discovered using small-scale hot-compression testing if careful consideration is given to the experimental setup, to determine the true deformation conditions.

5. Conclusions

Despite the convenience and popularity of the processing map approach, there are inherent issues with the methodology. The use of high temperature uniaxial compressive tests leads to deformation inhomogeneity in the sample during the test, which affects the measured stress-strain response and creates microstructural inhomogeneity in the sample. Because the deformation inhomogeneity depends on the experimental conditions like the thermal gradient in the sample and the friction at the platens, the measured stress strain curves are inherently difficult to reproduce. Because the calculation of strain rate sensitivity relies on fitting data from different temperatures separately, using a cubic polynomial, it is very sensitive to noise in the data. The procedure overfits the data, which is particularly problematic when the samples are tested at only 4 or 5 different strain rates and without repeat. For Zr-2.5Nb deformed in the $\alpha + \beta$ region, there seems to be only a gradual increase in strain rate sensitivity with increasing temperature and decreasing strain rate. Because of the deformation gradients in the sample, it is difficult to link microstructure evolution to processing conditions without a rigorous FE analysis of the tests. Thus, although the processing map methodology appears to be a fast method of identifying optimum processing conditions, it requires a highly detailed analysis of

the test, to improve reproducibility and to make the best of a large dataset of thermomechanical testing regimes.

Acknowledgements

This research was sponsored by Rolls-Royce plc. and was funded by *LightForm*, a UK Engineering and Physical Sciences Research Council (EPSRC) programme grant (EP/R001715/1).

References

[1] K.L. Murty, Applications of Crystallographic Textures of Zirconium Alloys in the Nuclear Industry, in: L.F.P. Van Swam, C.M. Eucken (Eds.), Zircon. Nucl. Ind. Eighth Int. Symp. ASTM STP 1023, American Society for Testing and Materials, Philadelphia, 1989: pp. 570–595.

[2] S. Banerjee, Nuclear Applications: Zirconium Alloys, in: K.H. Cahn, R.W. Flemings, B. Ilschner, E.J. Kramer, S. Mahajan, P. Veyssière (Eds.), Encycl. Mater. Sci. Technol., Elsevier Science Ltd., 2001: pp. 6287–6299. doi:10.1016/B0-08-043152-6/01117-7.

[3] C.S. Daniel, P.D. Honniball, L. Bradley, M. Preuss, J. Quinta da Fonseca, Texture Development during Rolling of α + β Dual-Phase ZrNb Alloys, in: R.J. Comstock, A.T. Motta (Eds.), Zircon. Nucl. Ind. 18th Int. Symp. ASTM STP1597, ASTM International, West Conshohocken, PA, 2017: pp. 151–179. doi:10.1520/STP159720160070.

[4] Y.V.R.K. Prasad, H.L. Gegel, S.M. Doraivelu, J.C. Malas, J.T. Morgan, K.A. Lark, D.R. Barker, Modeling of dynamic material behavior in hot deformation: Forging of Ti-6242, Metall. Trans. A. 15 (1984) 1883–1892. doi:10.1007/BF02664902.

[5] Y.V.R.K. Prasad, S. Sasidhara, Hot Working Guide: A Compendium of Processing Maps, 1st Editio, ASM International, 1997.

[6] S. Ghosh, Interpretation of microstructural evolution using dynamic materials modeling, Metall. Mater. Trans. A. 31 (2000) 2973–2974.

[7] J.K. Chakravartty, Y.V.R.K. Prasad, M.K. Asundi, Processing map for hot working of alpha-zirconium, Metall. Trans. A. 22 (1991) 829–836. doi:10.1007/BF02658992.

[8] J.K. Chakravartty, Y.V.R.K. Prasad, M.K. Asundi, Processing Map and Hot Working Characteristics of Zircaloy-2, in: C.M. Eucken, A.M. Garde (Eds.), Zircon. Nucl. Ind. Ninth Int. Symp. ASTM STP 1132, American Society for Testing and Materials,

Philadelphia, 1991: pp. 48–61.

[9] A. Sarkar, J.K. Chakravartty, Hot deformation behavior of Zr–1Nb alloy: Characterization by processing map, J. Nucl. Mater. 440 (2013) 136–142. doi:10.1016/j.jnucmat.2013.04.080.

[10] Y.B. Tan, L.H. Yang, C. Tian, R.P. Liu, X.Y. Zhang, W.C. Liu, Hot deformation behavior of ZrTiAlV alloy with a coarse grain structure in the β phase field, Mater. Sci. Eng. A. 577 (2013) 218–224. doi:10.1016/j.msea.2013.04.056.

[11] K.K. Saxena, S.D. Yadav, S. Sonkar, V. Pancholi, G.P. Chaudhari, D. Srivastava, G.K. Dey, S.K. Jha, N. Saibaba, Effect of Temperature and Strain Rate on Deformation Behavior of Zirconium Alloy: Zr-2.5Nb, Procedia Mater. Sci. 6 (2014) 278–283. doi:10.1016/j.mspro.2014.07.035.

[12] J.K. Chakravartty, R. Kapoor, A. Sarkar, V. Kumar, S.K. Jha, N. Saibaba, S. Banerjee, Identification of Safe Hot-Working Conditions in Cast Zr-2.5Nb, Zircon. Nucl. Ind. 17th Vol. (2015) 259–281. doi:10.1520/STP154320120197.

[13] J.K. Chakravartty, S. Banerjee, Y.V.R.K. Prasad, M.K. Asundi, Hot-working characteristics of Zircaloy-2 in the temperature range of 650–950°C, J. Nucl. Mater. 187 (1992) 260–271. doi:10.1016/0022-3115(92)90506-G.

[14] J.K. Chakravartty, S. Banerjee, Y.V.R.K. Prasad, Superplasticity in β-zirconium: A study using a processing map, Scr. Metall. Mater. 26 (1992) 75–78. doi:10.1016/0956-716X(92)90372-L.

[15] J.K. Chakravartty, G.K. Dey, S. Banerjee, Y.V.R.K. Prasad, Characterization of hot deformation behaviour of Zr-2.5Nb-0.5Cu using processing maps, J. Nucl. Mater. 218 (1995) 247–255. doi:10.1016/0022-3115(94)00379-3.

[16] J.K. Chakravartty, G.K. Dey, S. Banerjee, Y.V.R.K. Prasad, Dynamic recrystallisation during hot working of Zr–2·5Nb: characterisation using processing maps, Mater. Sci. Technol. 12 (1996) 705–716. doi:10.1179/026708396790122431.

[17] R. Kapoor, J.K. Chakravartty, Characterization of hot deformation behaviour of Zr–2.5Nb in β phase, J. Nucl. Mater. 306 (2002) 126–133. doi:10.1016/S0022-3115(02)01290-4.

[18] R. Kapoor, J.K. Chakravartty, C.C. Gupta, S.L. Wadekar, Characterization of superplastic behaviour in the (α+β) phase field of Zr–2.5wt.%Nb alloy, Mater. Sci. Eng. A. 392 (2005) 191–202. doi:10.1016/j.msea.2004.09.023.

[19] J.K. Chakravartty, R. Kapoor, S. Banerjee, Y.V.R.K. Prasad, Characterization of hot deformation behavior of Zr–1Nb–1Sn alloy, J. Nucl. Mater. 362 (2007) 75–86.

doi:10.1016/j.jnucmat.2006.11.007.

[20] J.K. Chakravartty, R. Kapoor, A. Sarkar, S. Banerjee, P. Barberis, S.W. Dean, Dynamic Recrystallization in Zirconium Alloys, J. ASTM Int. 7 (2010) 121–149. doi:10.1520/JAI103003.

[21] Y.V.R.K. Prasad, T. Seshacharyulu, S.C. Medeiros, W.G. Frazier, Effect of Prior β-Grain Size on the Hot Deformation Behavior of Ti-6Al-4V: Coarse vs Coarser, J. Mater. Eng. Perform. 9 (2000) 153–160. doi:10.1361/105994900770346097.

[22] T. Seshacharyulu, S.C. Medeiros, W.G. Frazier, Y.V.R.K. Prasad, Hot working of commercial Ti–6Al–4V with an equiaxed α–β microstructure: materials modeling considerations, Mater. Sci. Eng. A. 284 (2000) 184–194. doi:10.1016/S0921-5093(00)00741-3.

[23] V.V. Balasubrahmanyam, Y.V.R.K. Prasad, Hot Deformation Mechanisms in Ti-5.5Al-1Fe Alloy, J. Mater. Eng. Perform. 10 (2001) 731–739. doi:10.1361/105994901770344629.

[24] T. Seshacharyulu, S.C. Medeiros, W.G. Frazier, Y.V.R.K. Prasad, Microstructural mechanisms during hot working of commercial grade Ti–6Al–4V with lamellar starting structure, Mater. Sci. Eng. A. 325 (2002) 112–125. doi:10.1016/S0921-5093(01)01448-4.

[25] L.J. Huang, L. Geng, A.B. Li, X.P. Cui, H.Z. Li, G.S. Wang, Characteristics of hot compression behavior of Ti–6.5Al–3.5Mo–1.5Zr–0.3Si alloy with an equiaxed microstructure, Mater. Sci. Eng. A. 505 (2009) 136–143. doi:10.1016/j.msea.2008.12.041.

[26] I. Sen, R.S. Kottada, U. Ramamurty, High temperature deformation processing maps for boron modified Ti–6Al–4V alloys, Mater. Sci. Eng. A. 527 (2010) 6157–6165. doi:10.1016/j.msea.2010.06.044.

[27] S. Ghosh, Interpretation of flow instability using dynamic material modeling, Metall. Mater. Trans. A. 33 (2002) 1569–1572. doi:10.1007/s11661-002-0081-x.

[28] F. Montheillet, J.J. Jonas, K.W. Neale, Modeling of dynamic material behavior: A critical evaluation of the dissipator power co-content approach, Metall. Mater. Trans. A. 27 (1996) 232–235. doi:10.1007/BF02647764.

[29] I. Weiss, F.H. Froes, D. Eylon, G.E. Welsch, Modification of alpha morphology in Ti-6Al-4V by thermomechanical processing, Metall. Trans. A. 17 (1986) 1935–1947. doi:10.1007/BF02644991.

[30] S.L. Semiatin, V. Seetharaman, I. Weiss, Flow behavior and globularization kinetics

during hot working of Ti–6Al–4V with a colony alpha microstructure, Mater. Sci. Eng. A. 263 (1999) 257–271. doi:10.1016/S0921-5093(98)01156-3.

[31] E.B. Shell, S.L. Semiatin, Effect of initial microstructure on plastic flow and dynamic globularization during hot working of Ti-6Al-4V, Metall. Mater. Trans. A. 30 (1999) 3219–3229. doi:10.1007/s11661-999-0232-4.

[32] S. Mironov, M. Murzinova, S. Zherebtsov, G.A. Salishchev, S.L. Semiatin, Microstructure evolution during warm working of Ti–6Al–4V with a colony-α microstructure, Acta Mater. 57 (2009) 2470–2481. doi:10.1016/j.actamat.2009.02.016.

[33] S. Zherebtsov, M. Murzinova, G. Salishchev, S.L. Semiatin, Spheroidization of the lamellar microstructure in Ti–6Al–4V alloy during warm deformation and annealing, Acta Mater. 59 (2011) 4138–4150. doi:10.1016/j.actamat.2011.03.037.

[34] S. Banerjee, Displacive and Diffusional Transformations of the Beta Phase in Zirconium Alloys, in: Zircon. Nucl. Ind. 17th Vol., ASTM International, 100 Barr Harbor Drive, PO Box C700, West Conshohocken, PA 19428-2959, 2015: pp. 23–51. doi:10.1520/STP154320130039.

[35] P.S. Davies, An Investigation of Microstructure and Texture Evolution in the Near-α Titanium Alloy Timetal 834, PhD thesis available online, University of Sheffield, 2009.

[36] P.S. Davies, B.P. Wynne, W.M. Rainforth, M.J. Thomas, P.L. Threadgill, Development of microstructure and crystallographic texture during stationary shoulder friction stir welding of Ti-6Al-4V, Metall. Mater. Trans. A Phys. Metall. Mater. Sci. 42 (2011) 2278–2289. doi:10.1007/s11661-011-0606-2.

[37] M. Humbert, F. Wagner, H. Moustahfid, C. Esling, Determination of the Orientation of a Parent β Grain from the Orientations of the Inherited α Plates in the Phase Transformation from Body-Centred Cubic to Hexagonal Close Packed, J. Appl. Crystallogr. 28 (1995) 571–576. doi:10.1107/S0021889895004067.

[38] M. Humbert, N. Gey, The calculation of a parent grain orientation from inherited variants for approximate (b.c.c.–h.c.p.) orientation relations, J. Appl. Crystallogr. 35 (2002) 401–405. doi:10.1107/S0021889802005824.

[39] C.S. Daniel, P.D. Honniball, L. Bradley, M. Preuss, J. Quinta da Fonseca, A detailed study of texture changes during alpha–beta processing of a zirconium alloy, J. Alloys Compd. 804 (2019) 65–83. doi:10.1016/j.jallcom.2019.06.338.

[40] C.S. Daniel, C.J. Peyton, J. Quinta da Fonseca, High Temperature Compression Studies of a Zr-2.5Nb Alloy using Deformation Dilatometer [Data set], Zenodo.

(2019). doi:10.5281/zenodo.3374512.

[41] P. Jedrasiak, H.R. Shercliff, Finite element modelling of small-scale hot deformation testing, Cambridge University Engineering Department Technical Report, CUED/C-MATS/TR.264, (2020).

[42] M. Hu, L. Dong, Z. Zhang, X. Lei, R. Yang, Y. Sha, Correction of Flow Curves and Constitutive Modelling of a Ti-6Al-4V Alloy, Metals (Basel). 8 (2018) 256. doi:10.3390/met8040256.

[43] J. Zhang, H. Di, Deformation heating and flow localization in Ti–15–3 metastable β titanium alloy subjected to high Z deformation, Mater. Sci. Eng. A. 676 (2016) 506–509. doi:10.1016/j.msea.2016.09.011.

[44] P. Honarmandi, M. Aghaie-Khafri, Hot Deformation Behavior of Ti–6Al–4V Alloy in β Phase Field and Low Strain Rate, Metallogr. Microstruct. Anal. 2 (2013) 13–20. doi:10.1007/s13632-012-0052-6.

[45] P. Wanjara, M. Jahazi, H. Monajati, S. Yue, J.-P. Immarigeon, Hot working behavior of near-α alloy IMI834, Mater. Sci. Eng. A. 396 (2005) 50–60. doi:10.1016/j.msea.2004.12.005.

Figures

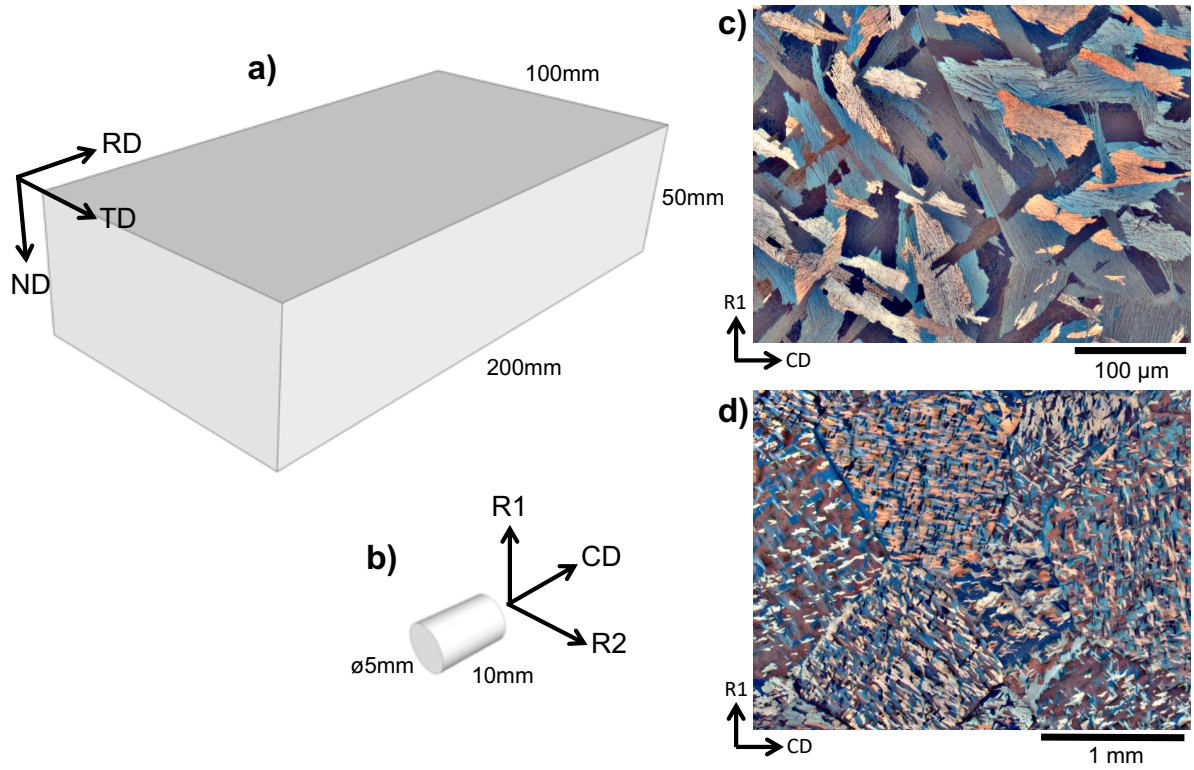

Figure 1: Schematic of the starting forged block of Zr-2.5Nb material (a) and a machined compression cylinder (b), showing orientation of the sample compression (CD) and radial (R1 and R2) directions relative to the rolled plate. The optical polarised light micrographs of the starting microstructure show packets of fine Widmanstätten α-laths (c), along with the outline of much larger prior-β grains (d).

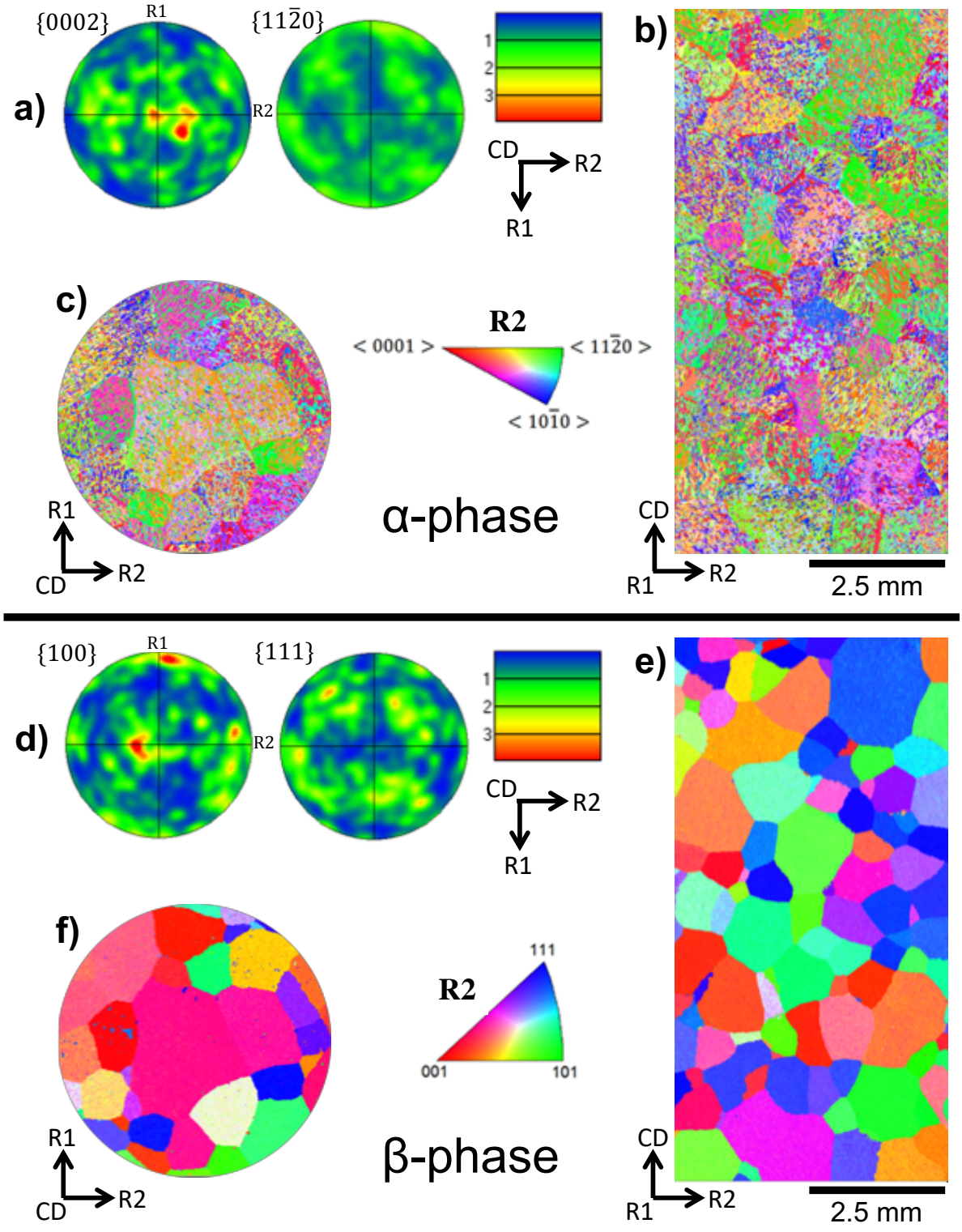

Figure 2: Analysis of starting α and β orientations within a compression sample. Pole figures, showing the texture measured over an area of 145 mm^2 at a step size of 5 µm, are plotted for the α-phase in (a) and β-phase in (d) with respect to the subsequent compression (CD) and radial (R1 and R2) directions. The orientation maps are shown as cross-sections of a compression sample, with many fine Widmanstätten α-laths in (b) and (c) and a number of larger β-grains appearing at high temperature in (e) and (f) which were reconstructed using a software algorithm.

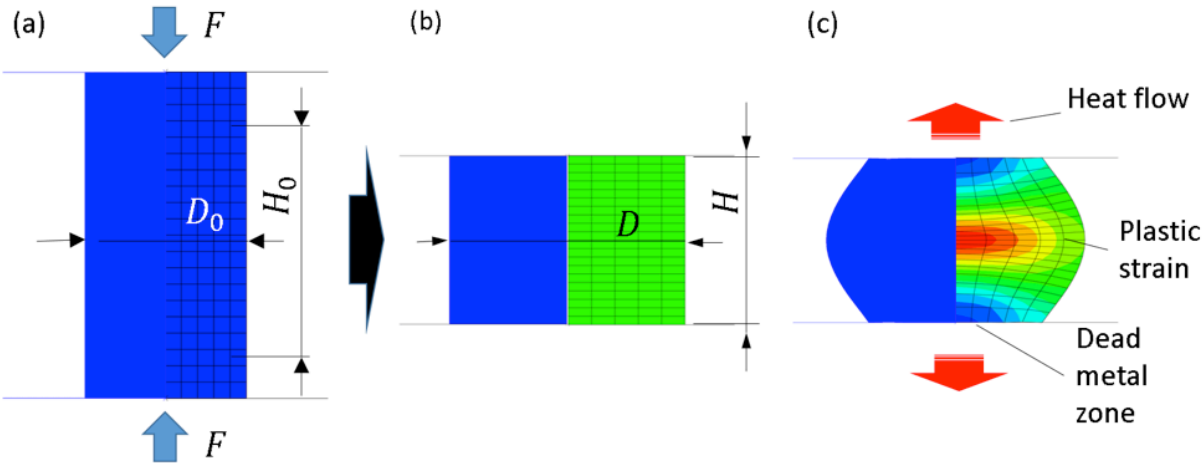

Figure 3: Sample shapes in hot-compression: (a) initial; (b) idealised homogeneous and frictionless; (c) predicted shape, showing barrelling due to friction and temperature gradient.

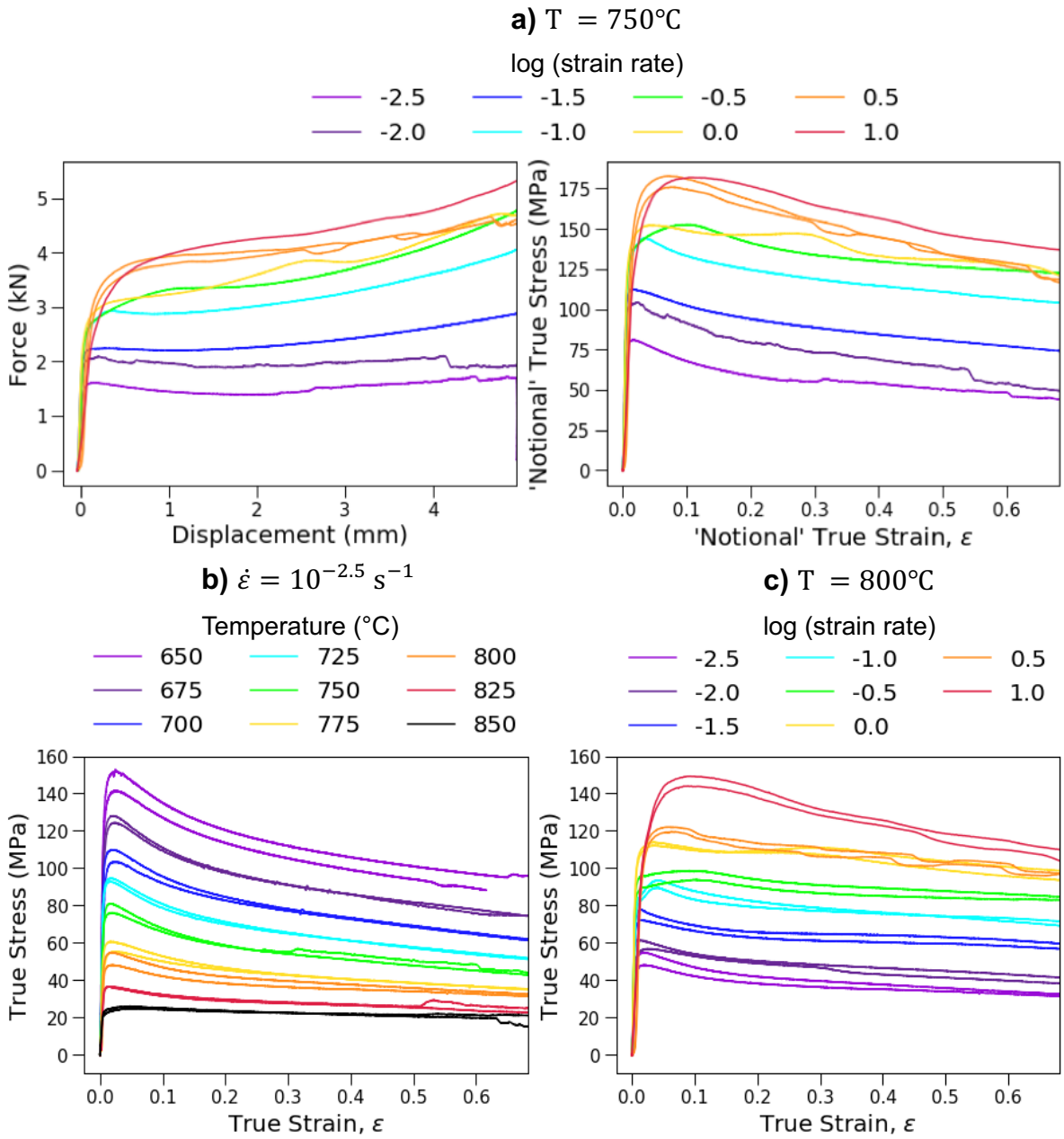

Figure 4: Sample force-displacement responses and corresponding 'notional' true stress-strain responses at a range of different strain-rates at 750°C (a). The effect of different temperatures, T, at a strain rate of $10^{-2.5}$ s^{-1} (b) and different strain rates, $\dot{\varepsilon}$, at a temperature of 800°C (c) on the measured 'notional' true stress-strain responses represent a sample of the flow stress data for Zr-2.5Nb in uniaxial compression recorded using the dilatometer.

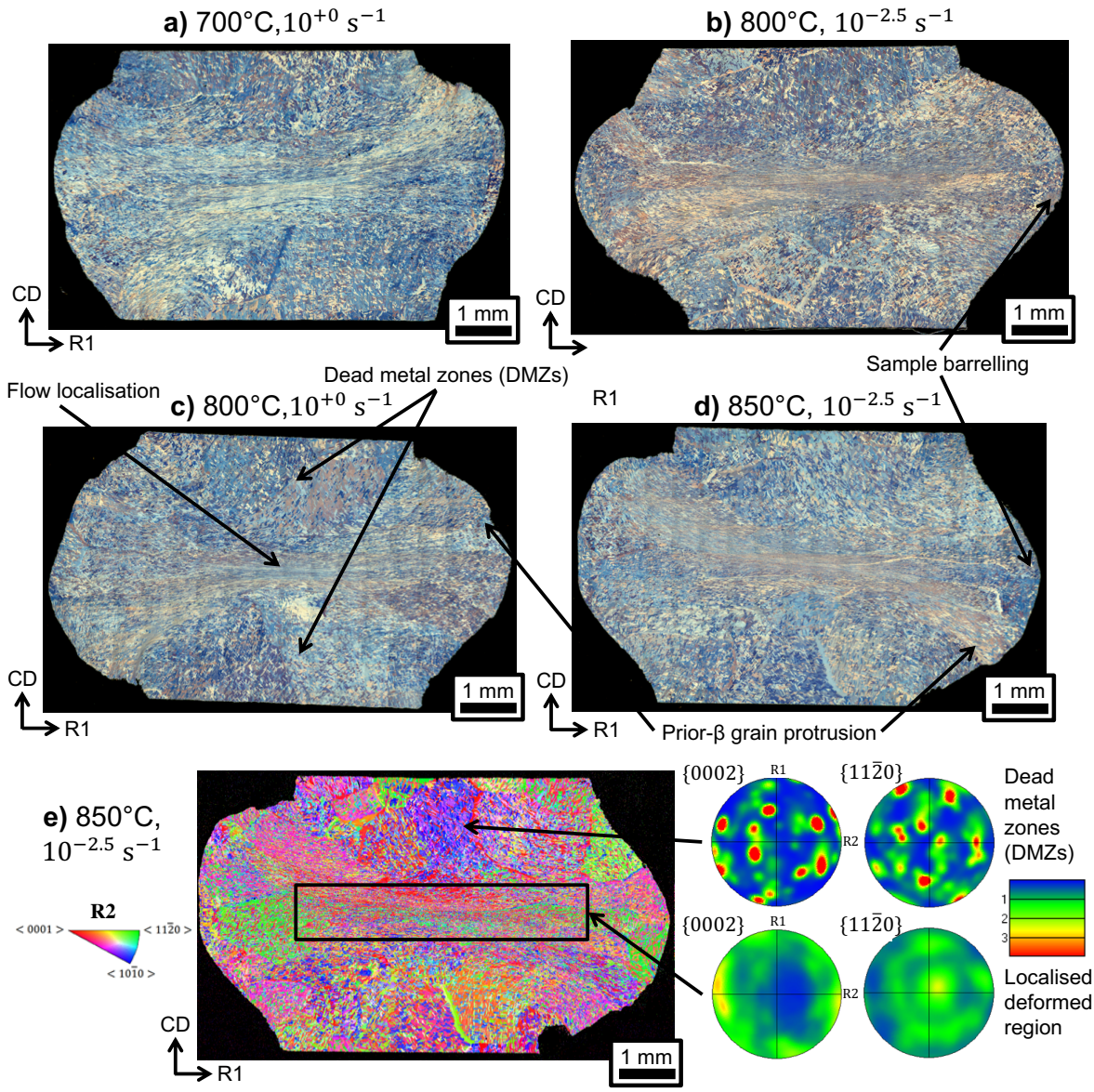

Figure 5: Optical polarised light micrographs of the Zr-2.5Nb compression samples after deformation at different temperatures and strain rates of (a) 700°C, 10^{+0} s^{-1}, (b) 800°C, $10^{-2.5}$ s^{-1}, (c) 800°C, 10^{+0} s^{-1} and (d) 850°C, $10^{-2.5}$ s^{-1}. The extent of flow localisation and barrelling is seen to increase with increasing temperature and decreasing strain rate. An α-phase orientation map shows dead metal zones (DMZs) at the top and bottom of the sample after deformation at 850°C, $10^{-2.5}$ s^{-1} in (e), along with crystallographic texture changes observed in the central deformed region.

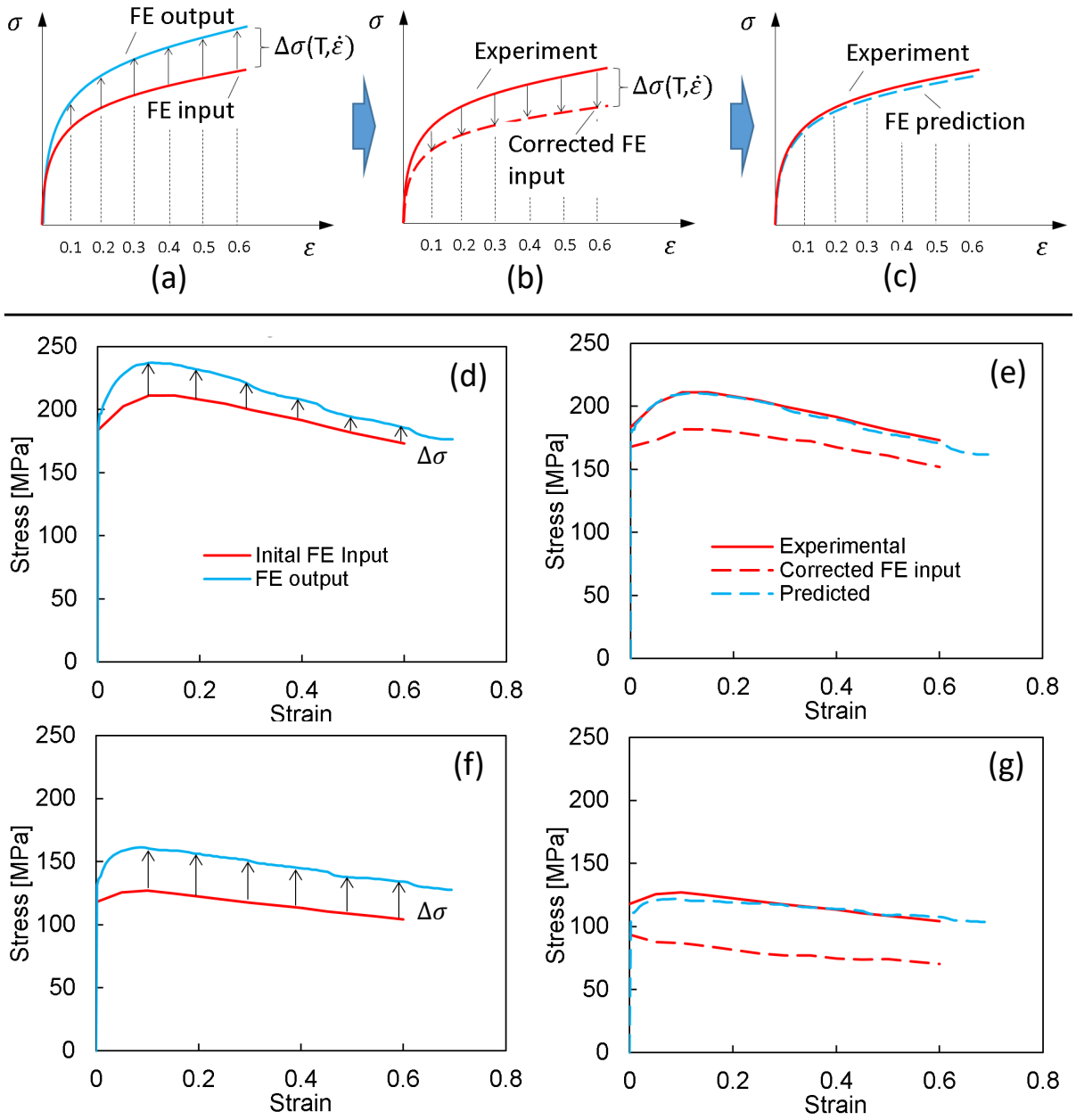

Figure 6: Methodology for correcting the true stress-strain response using the FE model: (a) taking an initial $\sigma = f(T, \dot{\varepsilon}, \varepsilon)$ from the 'notional' experimental data as input and determining a correction $\Delta\sigma(T, \dot{\varepsilon})$ from the FE output; (b) applying correction $\Delta\sigma(T, \dot{\varepsilon})$ to the experimental data; (c) validating the corrected FE input by matching the FE prediction with the experiment. FE modelling of true stress-strain curves for two temperature/strain-rate combinations: (d and e) 700°C, $10^{+0.5}$ s^{-1} and (f and g) 800°C, $10^{+0.5}$ s^{-1}, show the initial input from the experiment (solid red), the resulting output (solid red), the corrected input (dashed red) and the resulting corrected output (dashed blue) responses. The offset, $\Delta\sigma$, indicated by the black arrows, is seen to vary with strain at the different conditions.

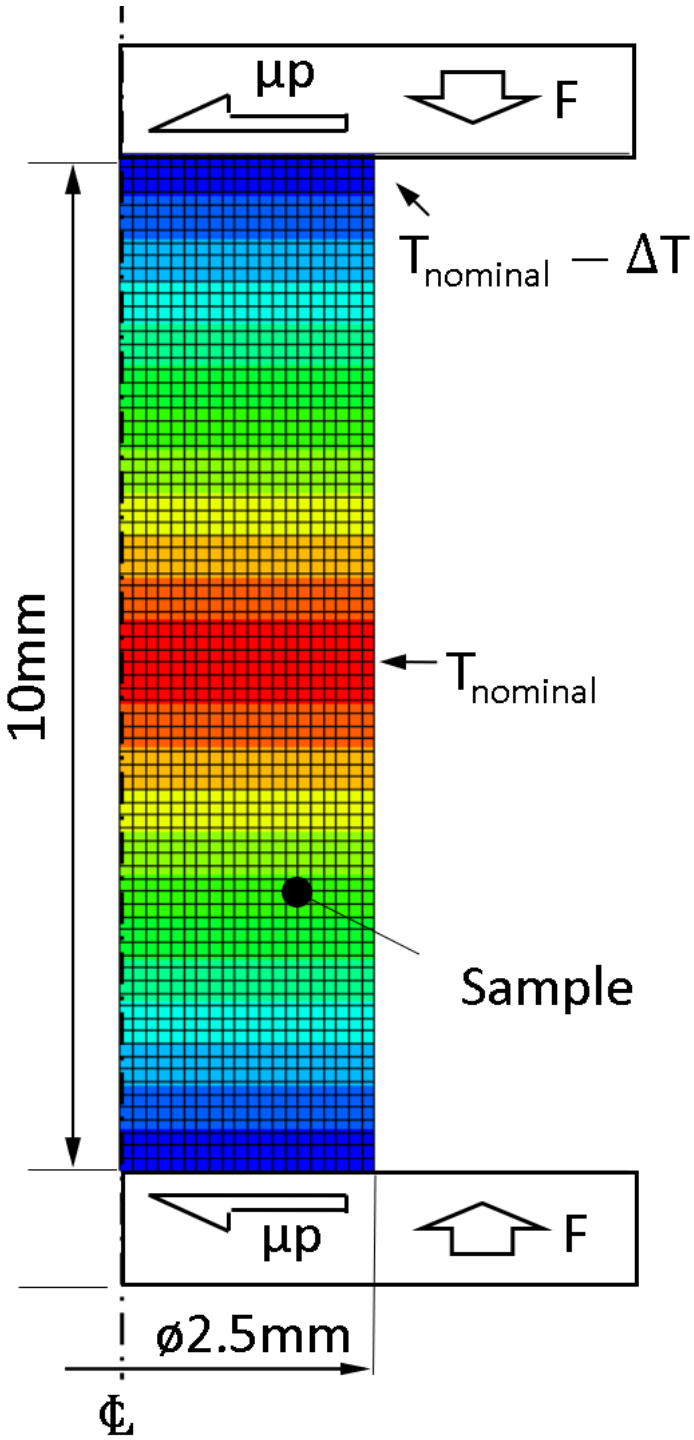

Figure 7: Finite element (FE) model, showing the axisymmetric mesh, geometry and boundary conditions. The compressive force is defined by F, and the friction force is defined by the product of the friction coefficient, μ, and the pressure, p. The temperature gradient is defined by a nominal temperature at the centre, T_{nominal}, and the temperature drop, ΔT.

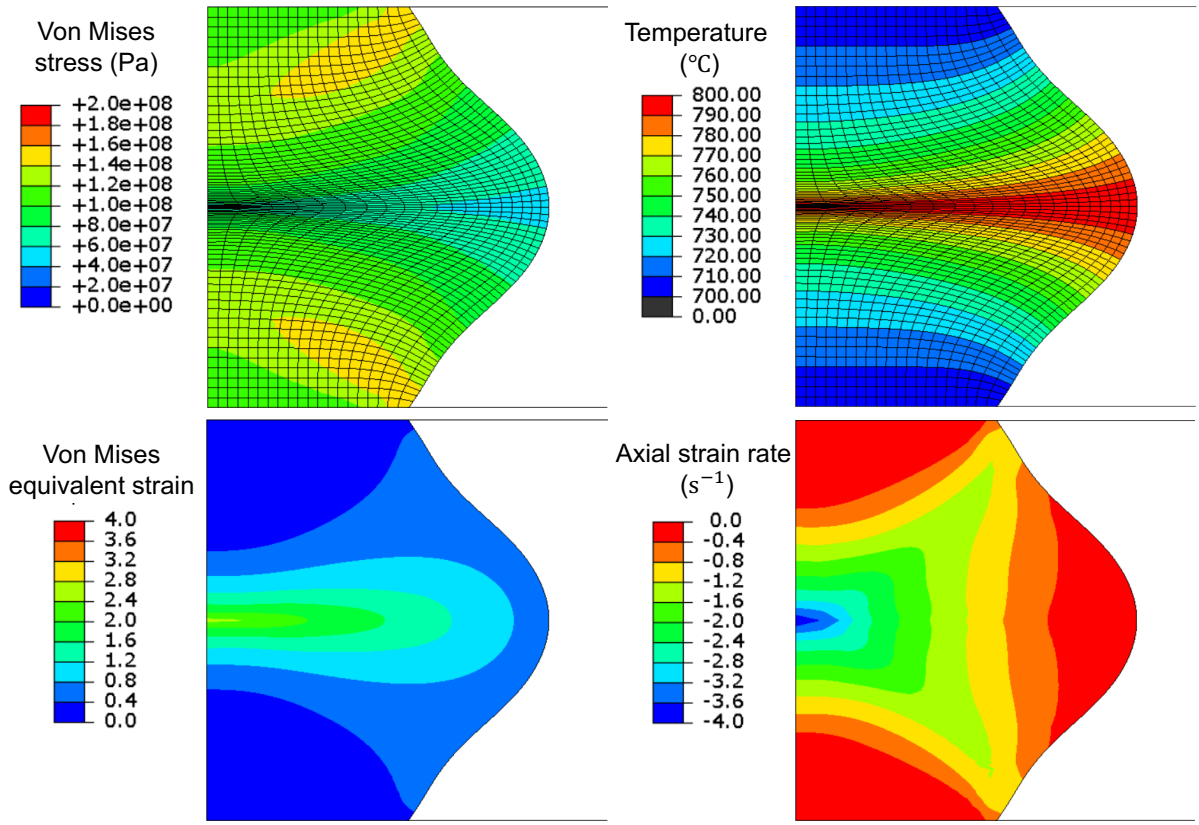

Figure 8: Contour maps of the FE predictions at the end of a test at an initial central temperature of 800°C and nominal strain-rate of 10^{+0} s^{-1}, showing equivalent von Mises stress and strain, temperature and axial strain-rate.

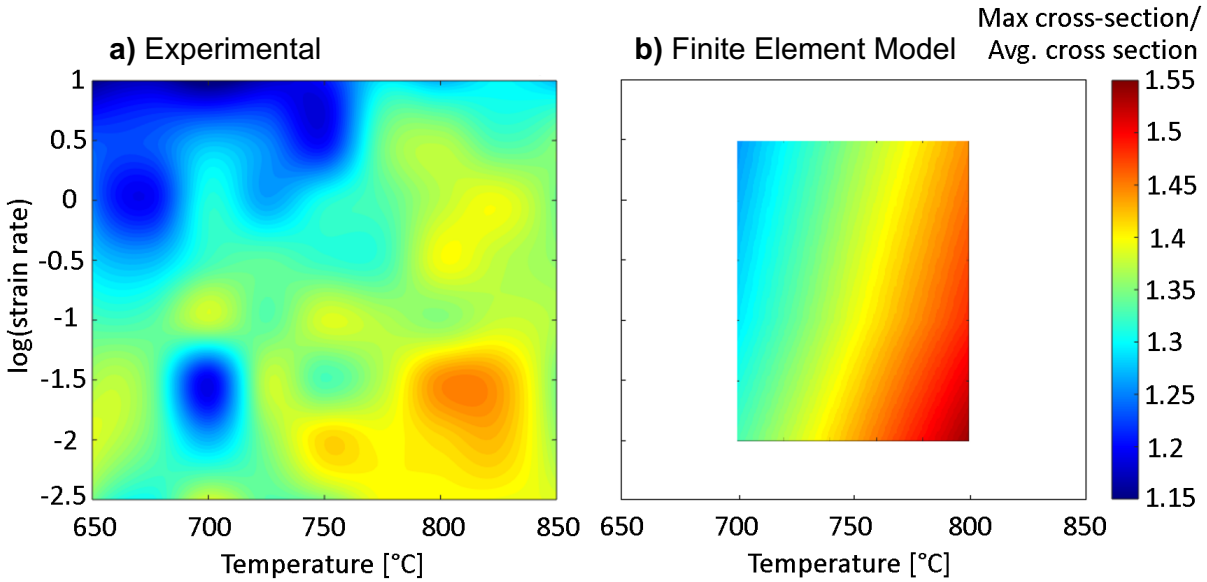

Figure 9: Heat maps of the cross-sectional area showing (a) experimentally measured barrelling and (b) barrelling predicted by the FE model.

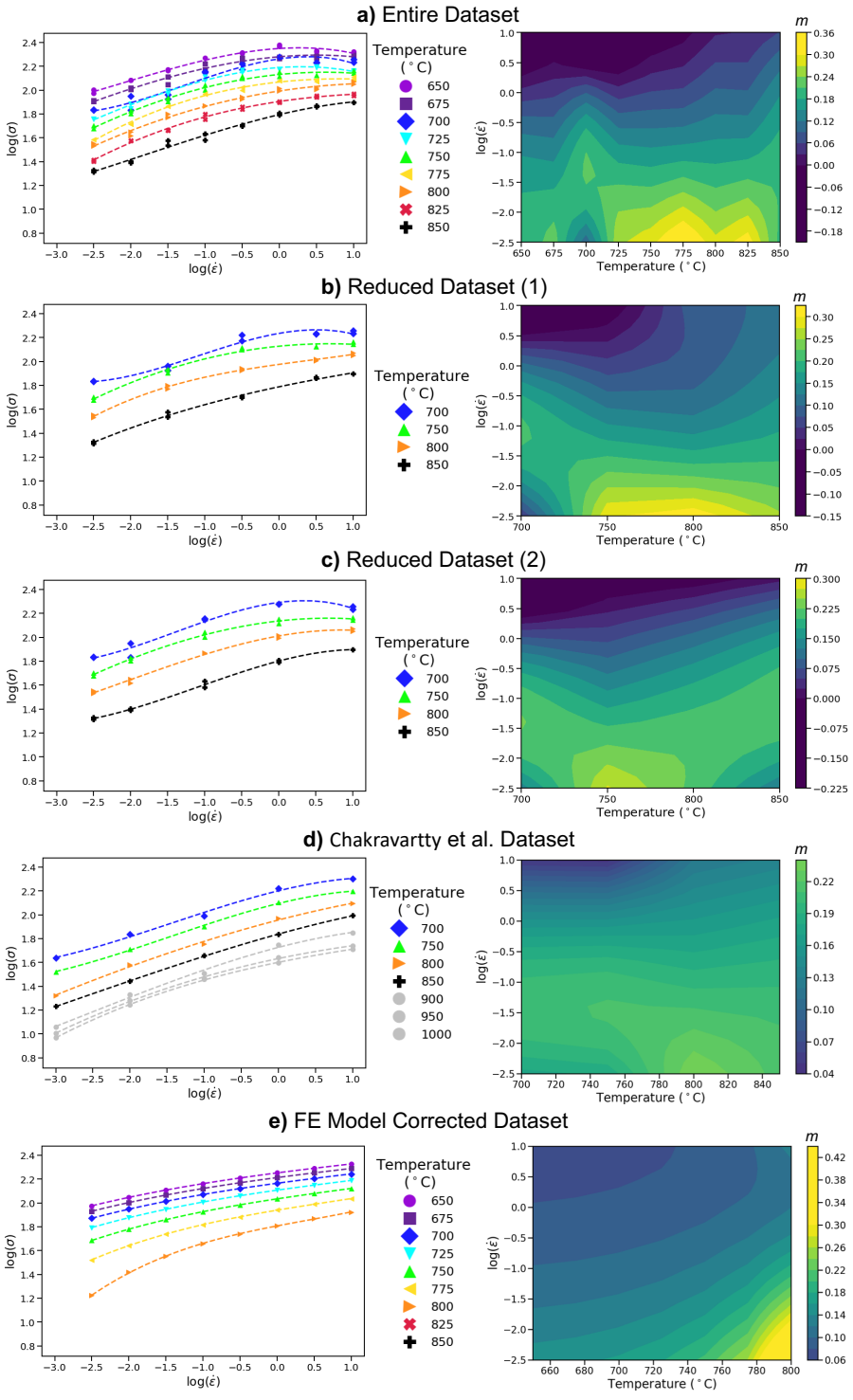

Figure 10: The development of processing maps for Zr-2.5Nb using experimental stress data at $\varepsilon = 0.5$. Showing (a) the entire dataset, plotted as log of stress versus log of strain rate data at each temperature, with the derivative of the cubic fit used to determine a contour map of strain rate sensitivity, m. Reducing the dataset in (b) and (c) sees different maxima and minima appear across the processing map, which differ in comparison with a previous study by Chakravartty et al. [12] in (d) and demonstrate the dependence of the results on the number of data points included in the study. The true material stress calculated from the FE model produces a corrected map in (e), which smooths out maxima and minima and shows only an increase in m at higher temperatures and lower strain rates.

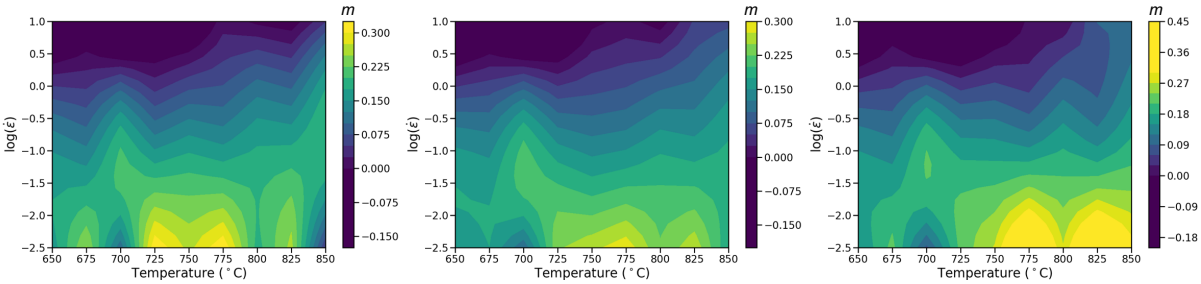

Figure 11: Analysis of the effect of ± 5 MPa random noise on the predictions of the experimental processing map. Showing different m maxima and minima appearing at different temperatures at low strain rate ($10^{-2.5}$ s^{-1}).

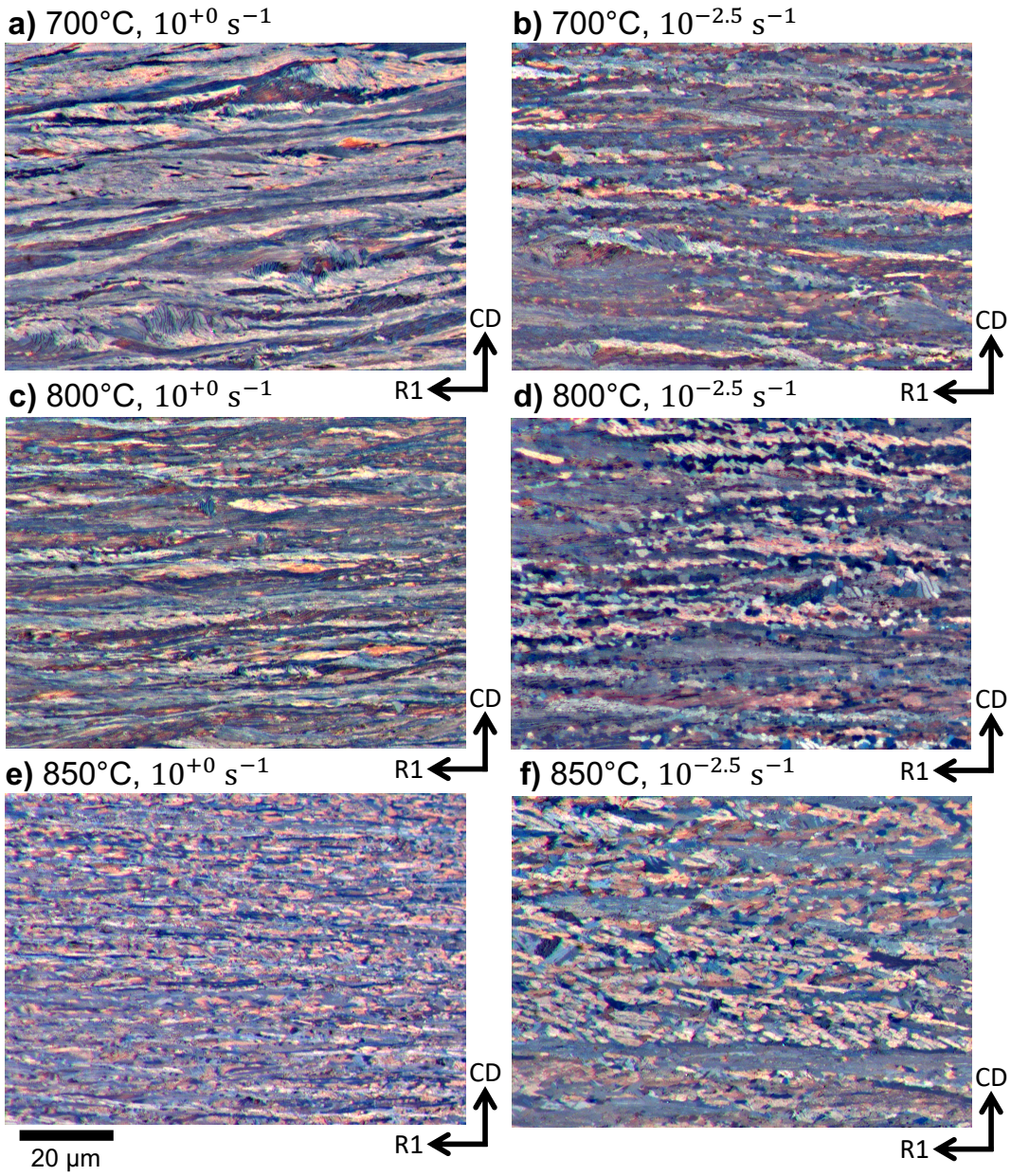

Figure 12: Optical polarised light micrographs at the centre of deformed Zr-2.5Nb compression samples. Showing differences in the α-grain structures at room temperature, following deformation at different temperatures and 'nominal' strain rates of (a) 700°C, 10^{+0} s^{-1}, (b) 700°C, $10^{-2.5}$ s^{-1}, (c) 800°C, 10^{+0} s^{-1}, (d) 800°C, $10^{-2.5}$ s^{-1}, (e) 850°C, 10^{+0} s^{-1} and (f) 850°C, $10^{-2.5}$ s^{-1}.

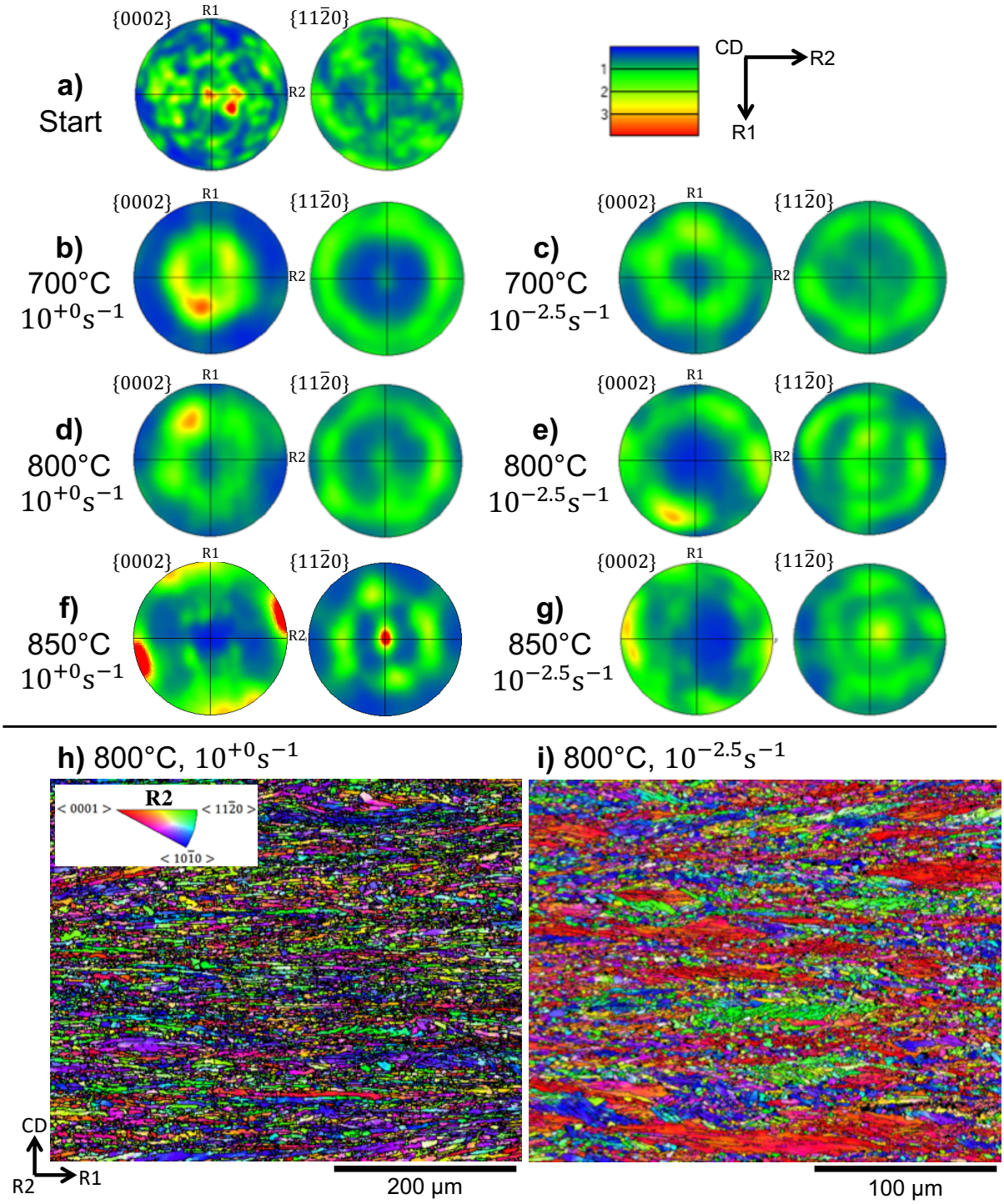

Figure 13: α-phase pole figures taken from the central deformed region of the Zr-2.5Nb compression samples. Showing the texture changes from (a) the starting material and after deformation at (b) 700°C, 10^{+0} s^{-1}, (c) 700°C, $10^{-2.5}$ s^{-1}, (d) 800°C, 10^{+0} s^{-1}, (e) 800°C, $10^{-2.5}$ s^{-1}, (f) 850°C, 10^{+0} s^{-1} and (g) 850°C, $10^{-2.5}$ s^{-1}. Fine α-phase orientation maps, at the centre of Zr-2.5Nb samples deformed at 800°C, show microstructures following deformation at an applied 'nominal' strain rate of 10^{+0} s^{-1} (h) and $10^{-2.5}$ s^{-1} (i). Much larger α-grains, with the 0002 basal pole oriented in the radial plane, appear following low strain rate deformation.